# Effect of ZnO Electron Extraction Layer on Charge Recombination and Collection Properties in Organic Solar Cells

Lan, Weixia; Liu, Yang; Wu, Bo; Xu, Bin; Pu, Huayan; Wei, Bin; Peng, Yan; Tian, Wenjing; ZHU, Fu Rong

*Published in:*
ACS Applied Energy Materials

*DOI:*
10.1021/acsaem.9b01383

Published: 28/10/2019

*Document Version:*
Peer reviewed version

# Effect of ZnO Electron Extraction Layer on Charge Recombination and Collection Properties in Organic Solar Cells

Weixia Lan[a,b], Yang Liu[c], Bo Wu[b], Bin Xu[c], Huayan Pu[a], Bin Wei[a], Yan Peng[a]*, Wenjing Tian[c]* , Furong Zhu[b]*

a) *School of Mechatronic Engineering and Automation, Shanghai University, Shanghai, 200072, China.*

b) *Department of Physics, Research Centre of Excellence for Organic Electronics, and Institute of Advanced Materials, Hong Kong Baptist University, 224 Waterloo Road, Kowloon Tong, Hong Kong, China*

c) *State Key Laboratory of Supramolecular Structures and Materials, Jilin University, 2699 Qianjin Street, Changchun 130012, China.*

Corresponding Author

*E-mail: pengyan@shu.edu.cn

*E-mail: wjtian@jlu.edu.cn

*E-mail: frzhu@hkbu.edu.hk

Keywords: Electron Extraction Layer, Charge Recombination, Charge Collection, Photo-CELIV, Organic Solar Cells

**Abstract**

The effect of zinc oxide (ZnO) electron extraction layer (EEL) on charge recombination and collection properties in bulk-heterojunction (BHJ) organic solar cells (OSCs), based on poly[[4,8-bis[(2-ethylhexyl)oxy] benzo [1,2-b:4,5-b'] dithiophene-2,6- diyl] [3-fluoro-2-[(2-ethylhexyl)carbonyl] thieno [3,4-b] thiophenediyl]] (PTB7):3'H-Cyclopropa[8,25] [5,6]fullerene-C70-D5h(6)-3'- butanoicacid, 3'-phenyl-, methyl ester ($PC_{70}BM$) blend system, has been analyzed using the transient photo-current (TPC) and photo-induced charge extraction by linearly increasing voltage (photo-CELIV) measurements. The TPC and photo-CELIV results indicate that the trap-limited bimolecular recombination can be strongly suppressed by interposing a 20 nm thick ZnO EEL between the BHJ and cathode, leading to a 9.4% increase in power conversion efficiency. The presence of ZnO EEL is beneficial in efficient operation of OSCs in two ways: (1) suppressing trap-limited bimolecular recombination and (2) enhancing the charge collection at the organic/cathode interface.

## Introduction

Remarkable progresses have been made in the development of high performing organic solar cells (OSCs) due to their characteristic advantages of flexibility, light weight and large-area solution fabrication capabilities.[1-3] Considerable efforts have been devoted to increase the power conversion efficiency (PCE) and the stability of OSCs through improved understanding of the impacts of the morphology, vertical stratification in bulk heterojunction (BHJ) on built-in potential ($V_{bi}$) in the devices.[4] Encouraging progresses made in OSCs with a PCE of >15% have been reported.[5] In a recent work, we show that maintaining a stable and high $V_{bi}$ across BHJ through interfacial modification favors the efficient and stable operation of OSCs.[6] The charge transport properties have a profound impact on charge recombination and charge collection in OSCs, which are the critical factors limiting the efficient operation of OSCs.[7] It is crucial to understand the charge transport, interfacial engineering and thus overcome the limitations for attaining high-performing and stable OSCs.

The loss of photo-generated carriers due to recombination includes monomolecular and bimolecular recombination processes. Monomolecular recombination, also known as the geminate recombination, is considered as the first order recombination process, where the charge transfer (CT) states originate from the same singlet excitons.[8,9] It was shown that the dissociation of the CT excitons is weakly dependent on the electric field in high performing OSCs.[10,11] With internal quantum efficiency approaching unity under short-circuit condition, it indicates that the bimolecular recombination process is a major loss mechanism in high-performance OSCs.[12-16]

Bimolecular recombination, or nongeminate recombination, is the recombination process that occurs between the photo-generated free electrons and holes before charge extraction, affecting especially the fill factor (FF).[17,18] It has been demonstrated that bimolecular recombination process is closely associated with the low charge carrier mobility in the disordered organic semiconductors and the charge trap states at the organic/electrode interface, leading to the buildup of space charges in BHJ, thus reducing the effective charge extraction probability.[19-23]

Interfacial engineering is one of the effective approaches for suppressing interfacial defects and improving the energy level alignment at the BHJ/electrode interfaces. This helps to minimize the recombination losses in OSCs.[24-27] The use of appropriate charge extraction interlayers also facilitates desired ohmic contact at the organic/electrode interface, avoiding the formation of unfavorable interface dipoles and carrier traps.[28,29] Various efforts have been devoted on the design of both electron extraction layer (EEL) (e.g., ZnO, LiF and poly[(9,9-bis(3'-(N,N-dimethylamino)propyl)- 2,7-fluorene)-alt-2,7-(9,9dioctylfluorene)] and hole extraction layer (HEL) (e.g., poly(3,4-ethylenedioxythiophene):poly (styrene sulphonate (PEDOT:PSS), $WO_3$, $V_2O_5$ and $MoO_3$). Among different EEL choices, ZnO is one of the most attractive materials due to its high optical transparency, high electron mobility and environmentally friendly attributes. It is also easy to synthesis and can be processed by cost-effective solution fabrication process.[30,31] There have been reports illustrating the great impact of ZnO morphology and surface properties on the cell performance.[32,33] The performance of OSCs is also dependent on the deposition of the ZnO EEL, including ZnO solution formulation,[34] process condition,[35] and post-deposition treatment.[36] However, much research

effort is desired to improve the understanding of charge recombination and collection properties for efficient and stable operation of OSCs.

In this work, the effect of ZnO EEL on charge collection and recombination properties has been analyzed systematically with a combination of photo-induced charge extraction by linearly increasing voltage (photo-CELIV), transient photo-current (TPC) and light intensity dependent current density–voltage (*J–V*) characteristic measurements. It shows that a 9.4 % increase in PCE of poly[[4,8-bis[(2-ethylhexyl)oxy] benzo [1,2-b:4,5-b'] dithiophene-2,6- diyl] [3-fluoro-2-[(2-ethylhexyl)carbonyl] thieno [3,4-b] thiophenediyl]] (PTB7):3'H-Cyclopropa[8,25] [5,6]fullerene-C70-D5h(6)-3'- butanoicacid, 3'-phenyl-, methyl ester ($PC_{70}BM$)-based OSCs with a 20 nm thick ZnO EEL as compared to a control OSC without a ZnO EEL. Our results suggest that the use of the ZnO EEL enables suppressing bimolecular recombination and unfavorable interfacial exciton dissociation, and thereby facilitating the sufficient charge extraction in OSCs.

**Device fabrication**

The ZnO nanoparticles with a diameter around 5.0 nm were synthesized following the processes described in a previous work.[37] The ZnO nanoparticle solution was formulated by mixing the ZnO particles in methanol (10 mg/ml). The PTB7:$PC_{70}BM$ solution was formulated by dissolving PTB7 (*1 Material)* and $PC_{70}BM$ (*Nano C*), mixed in a weight ratio of 1:1.5, in chlorobenzene (CB) solvent (Sigma-Aldrich, 99.8%), with a 3% 1, 8-Diiodooctane (DIO) (Sigma-Aldrich) additive. The donor/acceptor mixture solution was stirred overnight at 60 °C for better dissolution.

OSCs comprising a layer configuration of ITO/PEDOT:PSS(30 nm)/PTB7:$PC_{70}BM$(90 nm)/ZnO(20 nm)/Al(100 nm) were prepared. A 30 nm thick PEDOT:PSS (Baytron PVP AI4083) was prepared on the pre-cleaned ITO substrate using spin-coating at a rotation speed of 2500 rpm following a post-annealing at 140°C in air for 10 min. A 90 nm thick PTB7:$PC_{70}BM$ blend layer was then formed on the surface of PEDOT:PSS, prepared using the PTB7:$PC_{70}BM$ mixture solution by spin-coating at 2000 rpm for 120 s inside the glovebox, having oxygen and moisture levels <0.1 ppm. After drying at room temperature for ~1h, a 20 nm thick ZnO layer was then overlaid on the PTB7:$PC_{70}BM$ active layer by spin-coating at 2500 rpm for 120 s. Finally, samples were transferred to an adjacent vacuum evaporator for the deposition of a 100 nm thick Al top contact. The control cells without the ZnO interlayer were also made for comparison studies.

In the TPC measurements, an Nd:YAG pulsed laser with a pulse duration of 5 ns and the wavelength of 355 nm was used. A set of devices comprising layer configurations of ITO/PEDOT:PSS(30 nm)/$PC_{70}BM$(400 nm)/Al (30 nm) (control) and ITO /PEDOT:PSS(30 nm)/$PC_{70}BM$(400 nm)/ZnO(20 nm)/Al (30 nm) were prepared for the photo-physics studies. The use of the 400 nm thick $PC_{70}BM$ layer helps suppressing the drift current, generated in the bulk of the $PC_{70}BM$ layer, allowing for analyzing the interfacial exciton dissociation process occurred at the organic/electrode interface. The use of a 30 nm thick semitransparent top Al contact enables analyzing the interfacial exciton dissociation process at the organic/Al interface.[38,39]

In the photo-CELIV measurements, a short laser pulse is used to create free charge carriers

in an organic active layer, followed by the extraction of free charge carriers using a linear voltage ramp.[40, 41] A set of devices comprising layer configurations of ITO/PEDOT:PSS(30 nm)/PTB7:$PC_{70}BM$(90 nm)/Al(100 nm) and ITO/PEDOT:PSS(30 nm)/PTB7:$PC_{70}BM$(90 nm)/ZnO(20 nm)/Al(100 nm) were prepared for the photo-CELIV studies. An offset voltage ($U_{offset}$) of 0.6 V was applied to compensate $V_{bi}$ for offsetting the internal electric field.

**Results and discussion**

The *J–V* characteristics measured for OSCs with a ZnO EEL and a control cell under AM 1.5G illumination (100 mW/cm$^2$) are plotted in Fig. 1(a). The absorption spectrum of the ZnO layer is shown in the Inset in Fig. 1(a). A summary of the cell parameters, averaged from more than 10 cells, is listed in Table 1. A higher FF of 0.73 was obtained for OSCs with a ZnO EEL, which is obviously higher than that of an optimized control cell (0.67), leading to a PCE of 7.69±0.2 %, with a 9.4% increase as compared to the control cell (7.03±0.2 %). As shown in Table 1, OSCs with a ZnO EEL also exhibit a relatively lower $R_S$ and higher $R_{SH}$ compared to a control cell, revealing the efficient charge transport and extraction properties in the cell. The use of the ZnO EEL also improved contact quality at the active layer/Al interface, leading to an obvious reduction in the leakage current, as shown in Fig. 1(b).

Fig. 2 shows the double logarithmic plot of the photocurrent ($J_{ph}$)– effective voltage ($V_{eff}$), $J_{ph}$–$V_{eff}$, characteristics measured for OSCs, where $J_{ph}$= $J_l$–$J_d$, $J_l$ is current measured under illumination, $J_d$ is the dark current, with $J_{sat}$ being the saturation photocurrent. $V_{eff}$ is the effective voltage across the cell, defined as the difference between the built-in potential $V_{bi}$ and the applied bias. Almost all the photo generated carriers can be collected at a high $V_{eff}$. The

charge recombination increases with decrease in $V_{eff}$, therefore not all the photo-generated carriers can be collected at low $V_{eff}$. The charge collection efficiency $P$ is a function of the intensity of the incident light, $I$ and $V_{eff}$, and can be expressed as follows:[42]

$$P(I,V_{eff}) = J_{ph}(I,V_{eff}) \Big/ J_{ph,sat}(I) \quad (1)$$

$J_{ph}$ becomes independent of the applied voltage and saturates at a high $V_{eff}$ (>0.5 V), where $P$ approaches unity and gives rise to almost 100% collection of the photo-generated charges.[43] In this regime, recombination is negligible while it becomes increasingly important at low $V_{eff}$. As shown in Fig. 2, $P$ decreases much slower in a ZnO modified device than that in a control cell at $V_{eff}$ <0.5 V, revealing enhanced charge collection efficiency.

Light intensity dependent $J$–$V$ characteristics measured for OSCs with a ZnO EEL and the control cell are investigated. There is a power law dependence of the photocurrent on light intensity, e.g., $J_{ph} \propto I^{\alpha}$.[44,45] The value of the exponent $\alpha$ is associated with the recombination loss. $\alpha$ is usually approaching unity in OSCs with an efficient charge collection process, while the loss of the photo-generated charges through recombination generally results in a smaller $\alpha$. As shown in Fig. 3, a unity $\alpha$ was obtained at high $V_{eff}$, suggesting an excellent charge collection process. As the charge mobility in organic materials is field dependent, less efficient charge extraction and collection would occur at low $V_{eff}$, leading to the charge recombination due to the space charge accumulation, and thereby a decrease in $\alpha$ can be observed in the $J_{ph}$-$I$ characteristics. As shown in Fig. 3, $\alpha$ of 0.67 was obtained for the control device at a low $V_{eff}$ of 0.085 V, while a higher $\alpha$ of 0.87 could still be remained in OSCs with a ZnO EEL at the same $V_{eff}$ due to the reduced charge recombination, and thereby attaining higher charge

extraction.

OSCs with a ZnO EEL and the control cell possess the identical anode/organic contact. The charge extraction behaviors at the BHJ/anode in both types of OSCs can be considered identical. Hence, the change in the variations in the $J_{ph}$–$V_{eff}$ and $J_{ph}$–$I$ characteristics can be considered mainly due to the difference in charge extraction behaviors at the organic/cathode interfaces in both types of OSCs. The results reveal that OSCs with a ZnO EEL had a much-reduced recombination loss as compared to the control cell at the organic/cathode interface. The effect of the ZnO EEL on internal electric field, charge recombination and extraction processes in OSCs was analyzed using the TPC and photo-CELIV measurements.

The exciton dissociation processes at the organic/cathode interfaces, a critical factor determining the performance in OSCs, was analyzed.[46,47] The transient photocurrent includes: (1) the field dependent drift current formed under the internal electric field, and (2) current generated due to the interfacial exciton dissociation at the organic/electrode interfaces, which is independent on the electric field. To better understand the exciton dissociation process, the drift current due to the exciton dissociated at the donor/acceptor interface is offset by applying an opposite external bias to compensate the internal field. Therefore, the information of kinetics of photo-generated carriers at organic/electrode interface can be analyzed by measuring the transient photocurrents ($I_{TPC}$) at different biases.

$I_{TPC}$ measured for the devices comprising layer configurations of ITO/PEDOT:PSS/$PC_{70}BM$(400 nm)/Al(30 nm) and ITO/PEDOT:PSS/$PC_{70}BM$(400 nm)/ZnO(20 nm)Al(30 nm) at different biases, with light incident from the semitransparent Al

contact, are plotted in Fig. 4 (a) and (b). The positive $I_{TPC}$ decays measured without external bias are always observed for both types of devices, which is predominantly contributed by the drift current. However, very unique $I_{TPC}$ behaviors are observed when a positive bias is applied. $V_{bi}$ decreases when a positive bias was applied to the devices. Therefore, the contribution in $I_{TPC}$ from the drift current will decrease, while that originated from the exciton dissociation will increase. A clear rapid negative signal for the control device is observed with the reverse bias from 0.3 V to 0.5 V, and then followed with a slower positive photocurrent. The negative transient current originates from exciton dissociation at the $PC_{70}BM$/Al interface, which is very sensitive to the interfacial properties. While the slower positive photocurrent comes from the photo-generated carriers that drift with $V_{bi}$ and decreases with the increase of the reverse bias. This negative $I_{TPC}$ suggests that the direction of the transient current created by the exciton dissociation at the $PC_{70}BM$/Al contact is opposite to that of the drift current. Thus, these photo-generated electrons must be compensated preferentially before the drifted electrons are collected by the cathode. The negative transient photocurrent comes from the exciton dissociation which is unfavorable for electron collection. However, with the presence of a ZnO EEL between $PC_{70}BM$ and Al, the rapid negative transient current due to the unfavorable interfacial exciton dissociation at the organic/Al interface can be eliminated, only a rapid positive transient current is observed at an external bias of 0.9V. The TPC results reveal clearly that the use of a ZnO EEL helps to remove the unfavorable interfacial exciton dissociation, and thereby enhances of the electron collection efficiency.[39]

TPC measured for the devices comprising different layer configurations of ITO/Al(10 nm)/$PC_{70}BM$/$MoO_3$/Ag and ITO/Al(10 nm)/ZnO(20 nm)/$PC_{70}BM$/$MoO_3$/Ag was also

analyzed. The measured transient photocurrents are plotted in Fig. 5. It is clear that the rapid negative peak, indicating an unfavorable exciton dissociation at the Al/$PC_{70}$ BM interface, was not seen in devices with a reverse configuration, which is independent on the ZnO EEL. This indicates that the interfacial exciton dissociation behaviors at the organic/Al interface are dependent on formation of the organic/metal interface, e.g., the depositing sequences of the organic layer and Al. When the organic/metal interface is formed by depositing the organic layer on the Al layer, a relatively clear metal/organic interface is expected. However, the interfacial defects and traps occurred when the organic/Al interface was formed by depositing Al on organic surface using thermal evaporation. The sub-gap states induced by the interfacial defects may allow electron transfer from Al to $PC_{70}$BM, caused by the unfavorable interfacial exciton dissociation. The presence of the ZnO EEL also serves as a good hole-blocking layer at the organic/Al interface, preventing the undesired exciton dissociation at the $PC_{70}$BM/Al interface. Schematic diagrams illustrating the processes of exciton dissociation at the $PC_{70}$BM /Al and $PC_{70}$BM /ZnO/Al interfaces are presented in Fig. 6 (a) and (b).

The influence of the ZnO EEL on bimolecular recombination process is analyzed using photo-CELIV measurements. Photo-CELIV is a powerful technique to investigate both the carrier mobility and recombination dynamics.[48,49] Fig. 7 presents the schematic illustration of the photo-CELIV method. A laser pulse is introduced to generate the photo-carriers. An offset bias ($U_{\text{offset}}$) is applied to compensate the built-in potential, forcing the charge carriers to remain in the device and recombine. After an adjustable delay of the laser pulse, the remaining charge carriers are extracted under the linearly increasing voltage pulse with a rising speed $A$, which is defined as $A = dU/dt$.

The maximum current due to photoexcitation ($\Delta j$) and the time taken to reach the extraction current maximum ($t_{max}$) can be estimated using the photo-CELIV transient currentss. The charge mobility ($\mu$) can then be calculated using equation (2):

$$\mu = \frac{2d^2}{3At^2_{max}\left[1+0.36\frac{\Delta j}{j(0)}\right]} \quad (2)$$

Equation (2) is corrected for the electric field re-distribution during the charge extraction process. The photo-CELIV transients are recorded for OSCs with a thin ZnO EEL and the control cell over a delay time range from 5 μs to 1000 μs. $U_{offset}$ was set at -0.6V, which is very close to $V_{bi}$ in the cell. Fig. 8 presents the typical photo-CELIV transients measured for OSCs using a delay time of 5 μs. The carrier mobility results, calculated with Equation (2), show that the effective carrier mobility $\mu$ in the device with a ZnO/Al cathode ($2.0\times10^{-3}$ $cm^2V^{-1}s^{-1}$) is a little higher than that of the control cell ($9.7\times10^{-4}$ $cm^2V^{-1}s^{-1}$). This reveals the efficient carrier transport in OSCs with a ZnO EEL.

According to the theory of dispersive recombination dynamics, the delay time dependent density of electrons $n(t)$, and density of holes $p(t)$, can be expressed by:[50]

$$n(t) = p(t) = \frac{n(0)}{1+(t/\tau_B)^{\gamma}} \quad (3)$$

where $n(0)$ is the initial carrier density, $t$ is the delay time and $\tau_B = \left[\frac{\gamma}{n(0)\beta_0}\right]^{1/\gamma}$ is the bimolecular recombination lifetime. The parameter $\gamma$ ($0< \gamma <1$) is denoted as the dispersion parameter, which is around 1 for a non-dispersive recombination. The dispersive recombination process often results in a smaller $\gamma$. Fig. 9(a) exhibits the delay time-dependent carrier density

characteristics, obtained by integrating the photo-CELIV transients over time. Solid curves in Fig. 9 (a) are the theoretical results calculated using equation (3), indicating that $n(t)$ derived by photo-CELIV measurements are in good agreement with the results obtained by the theoretical recombination model. The values of $n(0)$, $\tau_B$ and $\gamma$, calculated for different cells, are summarized in Table 2. The carrier density includes the extracted photo-generated charge carriers remained after the recombination losses. The number of the extracted carriers varies with the delay time that was used in the photo-CELIV measurements.

Two particularities can be attained from the delay time dependent carrier density results. First, the density of extracted charge carriers decreases with increase in the delay time for both devices. This reflects that less photogenerated carriers were collected when longer delay time is applied due to the recombination processes. Second, the two devices exhibit very different delay time-dependent carrier density characteristics. The fitting data suggest the power law dependence of the carrier density on delay time for the control device. While for OSCs with a ZnO EEL, $n$(t) exhibits a much faster decay with increasing delay time, suggesting a higher order delay time dependence on carrier density. A smaller dispersive parameter $\gamma$ value ($\gamma$ =0.26) implies that a highly dispersive recombination process dominates in the control cell, indicating a high loss due to the trap-limited charge recombination. Whereas a high $\gamma$ of 0.98 manifests an almost non-dispersive or trap-free recombination in OSCs with a ZnO EEL.

According to the delay time-dependent bimolecular recombination relation $\frac{dn}{dt} = \frac{dp}{dt} = -\beta(t)np$, the bimolecular recombination coefficient $\beta(t)$ as a function of carrier density $n(t)$ can be expressed as follows:

$$\beta(t) = \frac{dn(t)/dt}{n^2(t)} \quad (4)$$

Combining equations (3) and (4), $\beta(t)$ can also be expressed as:

$$\beta(t) = a\gamma n_0^{-1}(at)^{\gamma-1} \quad (5)$$

where $a$=1/$\tau_B$,$\tau_B$is the "effective" bimolecular recombination lifetime ($\tau_B = \{\frac{\gamma}{[n(0)\beta_0]}\}^{1/\gamma}$), and γ (0＜γ≤1) is the dispersion parameter.

The relationship between $\beta(t)$ and $t$ can then be obtained by substituting $n(0)$, $\tau_B$ and $\gamma$ into equation (5), which is presented in Fig. 9(b). Results reveal different power law dependences between $\beta(t)$ and delay time for the two cells. $\beta(t)$ is almost independent on the delay time in ZnO modified device, with a constant value around $1.1\times10^{-11}$ $cm^3s^{-1}$. While for the control device, it declines quickly with an increase in the delay time. $\beta(t)$ decreased by two orders of magnitude when the delay time increased from 5 μs to 100 μs.

The disparate behaviors of delay time-dependent carrier concentration and bimolecular recombination coefficient can be explained with the multi-trapping model as illustrated in Fig. 10. For the control cell, Al was evaporated directly onto the surface of organic layer. The weak van der Waals interaction between molecules in the organic layer can be perturbated by the incoming flux of high energetic Al clusters during the thermal evaporation, inducing undesired interfacial traps due to the formation of the structural and energetic disorders in the organic layer. The incoming flux of the energetic Al clusters may also penetrate into the organic active layer, resulting in complex interfacial properties.[39] These influences will bring more interfacial defects and much deeper trap states in the active layer. The trapping and de-trapping processes

are responsible for the trap-limited bimolecular recombination.

Both the deep traps and shallow traps the charge carriers at a high carrier density trap. While, at a low carrier density, charge carriers trapped by the deep traps are more difficult to release. The charge carriers release from the shallow traps are mainly responsible for bimolecular recombination followed by the charge carriers de-trapped from the deep traps. The presence of the deeper traps or energy barriers at the organic/Al interface can lead to the buildup of the space charge, reducing the effective recombination rate. When a solution-processed ZnO layer is deposited before the thermal evaporation of Al, it can help to protect the active layer by reducing the numbers of the interfacial defects, which is beneficial for the trap-free bimolecular recombination with constant recombination rate.

## Conclusions

The effect of ZnO EEL on charge collection and recombination processes in PTB7:$PC_{70}BM$-based OSCs with a ZnO EEL has been analyzed systematically using a combination of photo-CELIV, light intensity dependent $J$–$V$ characteristic and TPC measurements. It shows that the use of the ZnO EEL favors the efficient operation of OSCs in two ways: (1) it helps to suppress the trap-limited bimolecular recombination, and (2) it enables to illuminate the unfavorable interfacial exciton dissociation at the organic/ cathode interface.

## Acknowledgements

The work was supported by the Research Grants Council, University Grants Committee of Hong Kong Special Administrative Region, China, General Research Fund (GRF/12302419),

Collaborative Research Fund (C5037-18GF), Hong Kong Baptist University Inter-institutional Collaborative Research Scheme (RC-ICRS/15-16/04), National Science Foundation of China (61827812 and 91648119), 973 Program (2014CB643506) and Program for Changbaishan Scholars of Jilin Province, China.

## References

(1) Tan, L.C.; Wang, Y.L.; Zhang, J.W.; Xiao, S.Q.; Zhou, H.Y.; Li, Y.W.; Chen, Y.W.; Li, Y.F. Highly Efficient Flexible Polymer Solar Cells with Robust Mechanical Stability. *Adv. Sci.* **2019**, 6, 1801180.

(2) Zhang, J.W.; Xu, G.Y.; Tao, F.; Zeng, G; Zhang, M.Y.; Yang, Y.; Li, Y.W.; Li, Y.F. Highly Efficient Semitransparent Organic Solar Cells with Color Rendering Index Approaching 100. *Adv. Mater.* **2019**, 31, 1807159.

(3) Wang, S.; Zhao, Y.; Lian, H.; Peng, C.; Yang, X.; Gao, Y.; Peng, Y.; Lan, W.X.; Elmi, O.L.; Stievenard, D.; Wei, B.; Zhu, F.R.; Xu, T. Towards All-solution-processed Top-illuminated Flexible Organic Solar Cells Using Ultrathin Ag-modified Graphite-coated Poly(ethylene terephthalate) Substrates. *Nanophotonics* **2019**, 8, 297-306.

(4) Wang, Y.W.; Wu, B.; Wu, Z.H.; Lan, Z.J.; Li, Y.F.; Zhang, M.J.; Zhu, F.R. Origin of efficient inverted nonfullerene organic solar cells: enhancement of charge extraction and suppression of bimolecular recombination enabled by augmented internal electric field, *J. Phys. Chem. Lett*. **2017**, 8, 5264-5271.

(5) Cui, Y.; Yao, H.F.; Zhang, J.Q.; Zhang, T.; Wang, Y.M.; Hong, L.; Xian, K.H.; Xu, B.W.; Zhang, Sh.Q.; Peng, J.; Wei, Z.X.; Gao, F.; Hou, J.H. Over 16% Efficiency Organic Photovoltaic Cells Enabled by a Chlorinated Acceptor with Increased Open-circuit Voltages. *Nat. Commun.* **2019**, 10, 2515.

(6) Wang, Y.W.; Lan, W.X.; Li, N.; Lan, Z.J.; Li, Z.; Jia, J.N.; Zhu, F.R. Stability of Nonfullerene Organic Solar Cells: from Built-in Potential and Interfacial Passivation Perspectives. *Adv. Energy Mater*. **2019**, 1900157.

(7) Lan, W.X.; Wang, Y.W.; Singh, J.; Zhu, F.R. Omnidirectional and Broadband Light Absorption Enhancement in 2‐D Photonic-Structured Organic Solar Cells. *ACS Photonics* 5, **2018**, 1144−1150.

(8) Hedley, G. J.; Ruseckas, A.; Samuel, I.D.W. Light Harvesting for Organic Photovoltaics. *Chem. Rev.* **2017**, 117, 796-837.

(9) Geng, Y.; Lee, M.H.; Troisi, A. Effect of Infrared Pulse Excitation on the Bound Charge-Transfer State of Photovoltaic Interfaces. *J. Phys. Chem. Lett.* **2017**, 8, 4872-4877.

(10) Kurpiers, J.; Neher, D. Dispersive Non-Geminate Recombination in an Amorphous Polymer:Fullerene Blend. *Sci. Rep.* **2016**, 6, 26832.

(11) Zusan, A.; Vandewal, K.; Allendorf, B.; Hansen, N.H.; Pflaum, J.; Salleo, A.; Dyakonov, V.; Deibel, C. The Crucial Influence of Fullerene Phases on Photogeneration in Organic Bulk Heterojunction Solar Cells. *Adv. Energy Mater.* **2014**, 4, 1400922.

(12) Jiang, W.; Jin, H.; Stolterfoht, M.; Shaw, P.E.;Nagiri, R. Loss Mechanisms in Fullerene-Based Low-Donor Content Organic Solar Cells. *J. Phys. Chem. C* **2018**, 122, 20611−20618.

(13) Göhler, C.; Wagenpfahl, A.; Deibel, C. Nongeminate Recombination in Organic Solar Cells. *Adv. Electron. Mater.* **2018** 1700505.

(14) Deibel, C.; Dyakonov, V. Polymer–fullerene Bulk Heterojunction Solar Cells. *Rep. Prog. Phys.* **2010**, 73, 096401.

(15) Burke, T.; Sweetnam, S.; Vandewal, K.; McGehee, M. Beyond Langevin Recombination: How Equilibrium between Free Carriers and Charge Transfer States Determines the Open-circuit Voltage of Organic Solar Cells. *Adv. Energy Mater*. **2015**, 1500123.

(16) Clarke, T.M.; Durrant, J.R. Charge Photogeneration in Organic Solar Cells. *Chem. Rev.* **2010**, 110, 6736-6767.

(17) Neher, D.; Kniepert, J.; Elimelech, A.; Koster, L. A New Figure of Merit for Organic Solar Cells with Transport-limited Photocurrents. *Sci. Rep.* **2016**, 6, 24861.

(18) Wurfel, U.; Neher, D.; Spies, A.; Albrecht, S. Impact of Charge Transport on Current–voltage Characteristics and Power-conversion Efficiency of Organic Solar Cells. *Nat. Commun.* **2015**, 6, 6951.

(19) Heiber, M.C.; Baumbach, C.; Dyakonov, V.; Deibel, C. Encounter-Limited Charge-Carrier Recombination in Phase-Separated Organic Semiconductor Blends. *Phys. Rev. Lett.* **2015**, 114, 136602.

(20) Nenashev, A.V.; Wiemer, M.; Dvurechenskii, A.V.; Gebhard, F.; Koch, M.; Baranovskii, S.D. Why the Apparent Order of Bimolecular Recombination in Blend Organic Solar Cells can be Larger than Two: A Topological Consideration. *Appl. Phys. Lett.* **2016**, 109, 033301.

(21) Gorenflot, J.; Heiber, M.C.; Baumann, A.; Lorrmann, J.; Gunz, M.; Kampgen, A.; Dyakonov, V.; Deibel,C. Nongeminate recombination in neat P3HT and P3HT:PCBM blend films. *J. Appl. Phys.* **2014**, 115, 144502.

(22) Chowdhury, M.; Sajjad, M.T.; Savikhin, V.; Hergue, N.; Sutija, K.B.; Oosterhout, S.D.; Toney, M.F.; Dubois, P.; Ruseckas, A.; Samuel, I. Tuning Crystalline Ordering by Annealing and Additives to Study its Effect on Exciton Diffusion in a Polyalkylthiophene Copolymer. *Phys. Chem. Chem. Phys.* **2017**, 19, 12441-12451.

(23) Zhang, R.Q.; Zhao, M.; Wang, Z.Q.; Wang, Z.T.; Zhao, B.; Yanqin Miao, Y.Q.; Zhou, Y.J.; Wang, H.; Hao, Y.Y.; Chen, G.; Zhu, F.R. Solution-Processable ZnO/Carbon Quantum Dots Electron Extraction Layer for Highly Efficient Polymer Solar Cells. *ACS Appl. Mater. Interfaces* **2018**, 10, 4895−4903.

(24) He, Z.; Zhong, C.; Su, S.; Xu, M.; Wu, H.; Cao, Y. Enhanced power-conversion efficiency in polymer solar cells using an inverted device structure. *Nat. Photonics* **2012**, 6, 591-595.

(25) Zhang, Z.; Qi, B.; Jin, Z.; Chi, D.; Qi, Z.; Li, Y.; Wang, J. Perylene Diimides: a Thickness-insensitive Cathode Interlayer for High Performance Polymer Solar Cells. *Energy Environ. Sci.* **2014**, 7, 1966-1973.

(26) Shah, S.K.; Hayat, K.; Ali, K. Effect of $TiO_2$ interlayer on the performance of inverted polymeric solar cells. *Mater. Res. Express* **2019**, 6, 065102.

(27) Bi, S.; Leng, X.; Li, Y.; Zheng, Z.; Zhang, X.; Zhang, Y.; Zhou, H. Interfacial Modification in Organic and Perovskite Solar Cells. *Adv. Mater.* **2018**, 1805708.

(28) Chen, S.; Manders, J.R.; Tsang, S.W.; So, F. Metal Oxides for Interface Engineering in Polymer Solar Cells. *J. Mater. Chem.* **2012**, 22, 24202-24212.

(29) Hwang, J.; Wan, A.; Kahn, A. Energetics of Metal–organic Interfaces: New Experiments and Assessment of the Field. *Mat. Sci. Eng. R* **2009**, 64, 1-31.

(30) Frankenstein, H.; Leng, C.Z.; Losego, M.D.; Frey, G.L. Atomic Layer Deposition of ZnO Electron Transporting Layers Directly onto the Active Layer of Organic Solar Cells. *Org. Electron.* **2019**, 64, 37-46.

(31) Babu, B.H.; Lyu, C.; Yu, C.; Wen, Z.; Li, F.; Hao, X.T. Role of Central Metal Ions in 8-Hydroxyquinoline-Doped ZnO Interfacial Layers for Improving the Performance of Polymer Solar Cells. *Adv. Mater. Interfaces* **2018**, 5, 1801172.

(32) Aqoma, H.; Park, S.; Park, H.Y.; Hadmojo, W.T.; Oh, S.H.; Nho, S.; Kim, D.H.; Seo, J. ; Park, S.; Ryu, D.Y.; Cho, S.; Jang, S.Y. 11% Organic Photovoltaic Devices Based on PTB7-Th: $PC_{71}BM$ Photoactive Layers and Irradiation-Assisted ZnO Electron Transport Layers. *Adv. Sci.* **2018**, 5, 1700858.

(33) Wei, J.; Ji, G.; Zhang, C.; Yan, L.; Luo, Q. ; Wang, C.; Chen, Q.; Yang, J.; Chen, L.; Ma, C. Q. Silane-Capped ZnO Nanoparticles for Use as the Electron Transport Layer in Inverted Organic Solar Cells. *ACS Nano* **2018**, 12, 5518-5529.

(34) Ghosh, M.; Ningthoujam, R.S.; Vatsa, R.K.; Das, D.; Nataraju, V.; Gadkari, S.C.; Gupta, S.K.; Bahadur, D. Role of Ambient Air on Photoluminescence and Electrical Conductivity of Assembly of ZnO Nanoparticles. *J. Appl. Phys.* **2011**, 110, 054309.

(35) Singh, S.; Chakrabarti, P. Comparison of the Structural and Optical Properties of ZnO Thin Films Deposited by Three Different Methods for Optoelectronic Applications. *Superlattice. Microst.* **2013**, 64, 283-293.

(36) Kuwabara, T.; Tamai, C.; Omura, Y.; Yamaguchi, T.; Taima, T.; Takahashi, K. Effect of UV Light Irradiation on Photovoltaic Characteristics of Inverted Polymer Solar Cells Containing Sol–gel Zinc Oxide Electron Collection Layer. *Org. Electron.* **2013**, 14, 649-656.

(37) Cheng, W.; Wu, Z.; Wen, S.; Xu, B.; Li, H.; Zhu, F.R. ;Tian, W.J. Donor–acceptor Copolymers Incorporating Polybenzo[1,2-*b*:4,5-*b*′]dithiophene and Tetrazine for High Open Circuit Voltage Polymer Solar Cells. *Org. Electron.* **2013**, 14 , 2124-2131.

(38) Wu, B.; Wu, Z.H. ; Yang, Q.Y.; Zhu, F.R. ; Ng, T.W.; Lee, C.S.; Cheung, S.H.; So, S.K. Improvement of Charge Collection and Performance Reproducibility in Inverted Organic Solar Cells by Suppression of ZnO Subgap States. *ACS Appl. Mater. Inter.* **2016**, 8, 14717-14724.

(39) Wu, B.; Wu, Z.H.; Tam, H.L.; Zhu, F.R. Contrary Interfacial Exciton Dissociation at Metal/organic Interface in Regular and Reverse Configuration Organic Solar Cells. *Appl. Phys. Lett.* **2014**, 105, 103302.

(40) Liu, Y.; Gao, Y.J.; Xu, B.; Loosdrecht, P.; Tian, W.J. Trap-limited Bimolecular Recombination in Poly(3-hexylthiophene):Fullerene Blend Films. *Org. Electron.* **2016**, 38, 8-14.

(41) Chellappan, V.; Ng, G. M.; Tan, M.J.; Goh, W.P.; Zhu, F.R. Imbalanced Charge Mobility in Oxygen Treated Polythiophene/fullerene Based Bulk Heterojunction Solar Cells. *Appl. Phys. Lett.* **2009**, 95, 263305.

(42) Kyaw, A.K.; Wang, D.H.; Gupta, V.; Leong, W.L.; Ke, L.; Bazan, G.C.; Heeger, A.J. Intensity Dependence of Current–Voltage Characteristics and Recombination in High-Efficiency Solution-Processed Small-Molecule Solar Cells. *ACS Nano* **2013**, 7, 4569-4577.

(43) Wu, Z.H.; Wu, B.; Tam, H.L.; Zhu, F.R. An Insight on Oxide Interlayer in Organic Solar Cells: From Light Absorption and Charge Collection Perspectives. *Org. Electron.* **2016**, 31, 266-272.

(44) Lan, W.X. Light Harvesting and Charge Collection in Bulk Heterojunction Organic Solar Cells (2016). Open Access Theses and Dissertations. https://repository.hkbu.edu.hk/cgi/viewcontent.cgi?amp=&article=1318&context=etd_oa

(45) Zhang, W.D.; Lan, W.X.; Lee, M.H.; Singh, J.; Zhu, F.R. A versatile solution-processed $MoO_3$/Au nanoparticles/$MoO_3$ hole contact for high performing PEDOT:PSS-free organic solar cells. *Org. Electrons*. **2018**, 52,1-6.

(46) Shuttle, C.G.; O'Regan, B.; Ballantyne, A.M.; Nelson, J.; Bradley, D.D.C.; Mello, J.; Durrant, J. R. Experimental Determination of the Rate Law for Charge Carrier Decay in a Polythiophene: Fullerene Solar Cell. *Appl. Phys. Lett.* **2008**, 92, 093311.

(47) Boix, P.P.; Ajuria, J.; Pacios, R.; Garcia-Belmonte, G. Carrier Rrecombination Losses in Inverted Polymer: Fullerene Solar Cells with ZnO Hole-blocking Layer from Transient Photovoltage and Impedance Spectroscopy Techniques. *J. Appl. Phys.* **2011**, 109, 074514.

(48) Yang, Y.; Chen, W.; Dou, L.; Chang, W. H.; Duan, H.S.; Bob, B.; Li, G.; Yang, Y. High-performance Multiple-donor Bulk Heterojunction Solar Cells. *Nat. Photon* **2015**, 9, 190-198.

(49) Park, H.J.; Lee, J.Y.; Lee, T.; Guo, L.J. Advanced Heterojunction Structure of Polymer Photovoltaic Cell Generating High Photocurrent with Internal Quantum Efficiency Approaching 100%. *Adv. Energy Mat.* **2013**, 3, 1135-1142.

(50) Mozer, A.J.; Dennler, G.; Sariciftci, N.S.; Westerling, M.; Pivrikas, A.; Österbacka, R.; Juška, G. Time-dependent Mobility and Recombination of the Photoinduced Charge Carriers in Conjugated Polymer/fullerene Bulk Heterojunction Solar Cells. *Phys. Rev. B* **2005**, 72, 035217.

Table of Graphic

Fig. 1: (a) $J$–$V$ and (b) dark $J$–$V$ characteristics measured for OSCs with a ZnO EEL and a control cell. Inset in Fig. 1(a): Absorption spectrum of the ZnO layer.

Fig. 2: Double logarithmic plots of $J_{Ph}$–$V_{eff}$ characteristics obtained for OSCs with a ZnO EEL and a control cell.

Fig. 3: Double logarithmic plots of the photocurrent density as a function of light intensity measured for (a) the OSC with a ZnO EEL and (b) a control cell under different effective voltages.

Fig. 4: Transient photocurrents measured for devices comprising layer configurations of (a) ITO/PEDOT:PSS/$PC_{70}BM$/Al and (b) ITO/PEDOT:PSS/$PC_{70}BM$/ZnO/Al under different external biases.

Fig. 5: Transient photocurrents measured for devices comprising layer configurations of (a) ITO/Al/$PC_{70}BM$/$M_OO_3$/Ag and (b) ITO/Al/ZnO/$PC_{70}BM$/$M_OO_3$/Ag under different external biases.

Fig. 6: Schematic diagrams illustrating the processes of interfacial exciton dissociation at the (a) organic/Al and (b) organic/ZnO/Al interfaces.

Fig. 7: Schematic illustration of the photo-CELIV method.

Fig. 8: Typical photo-CELIV transients measured for the OSC with a ZnO EEL and a control cell with a delay of 5 μs.

Fig. 9: Double logarithmic plots of delay time-dependent (a) carrier concentration and (b) bimolecular recombination coefficient obtained for the OSC with a ZnO EEL and a control cell.

Fig. 10: Schematic diagram illustrating the multi-trap model and the distribution of the interfacial defects and traps formed at the organic/Al interface that is formed by depositing Al on (a) organic layer, and (b) on ZnO EEL-protected organic layer.

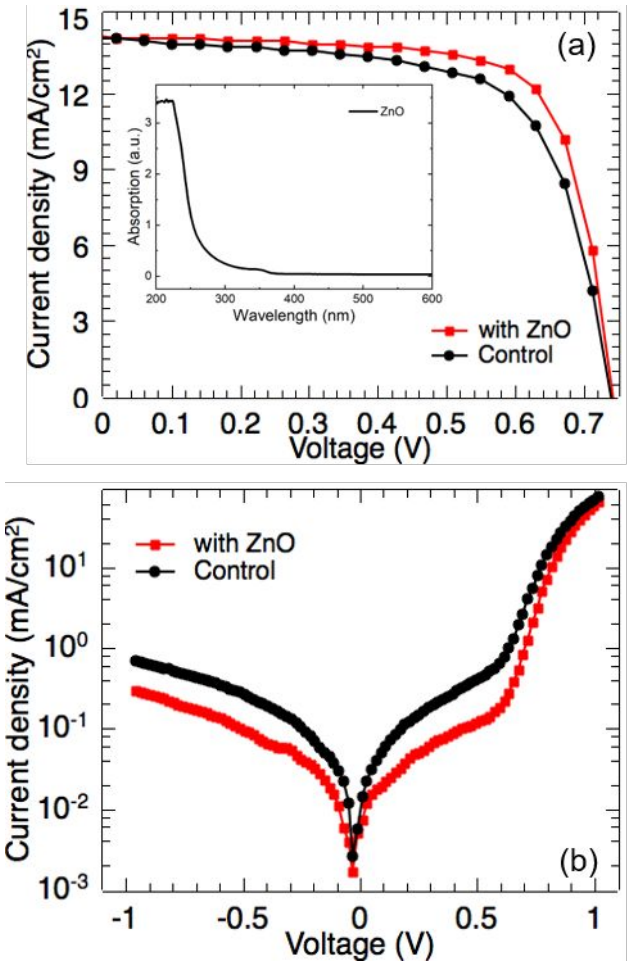


Fig. 1: (a) *J–V* and (b) dark *J–V* characteristics measured for OSCs with a ZnO EEL and a control cell. Inset in Fig. 1(a): Absorption spectrum of the ZnO layer.

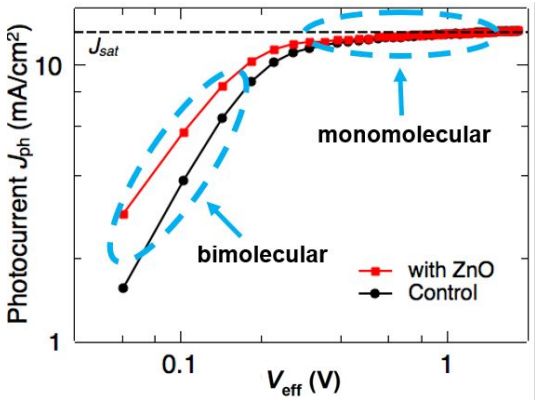


Fig. 2: Double logarithmic plots of $J_{Ph}$–$V_{eff}$ characteristics obtained for OSCs with a ZnO EEL and a control cell.

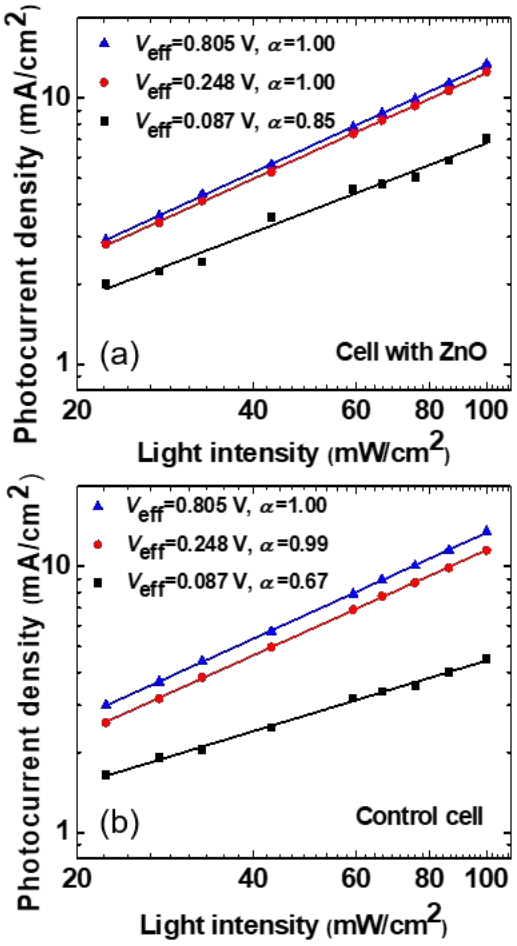


Fig. 3: Double logarithmic plots of the photocurrent density as a function of light intensity measured for (a) the OSC with a ZnO EEL and (b) a control cell under different effective voltages.

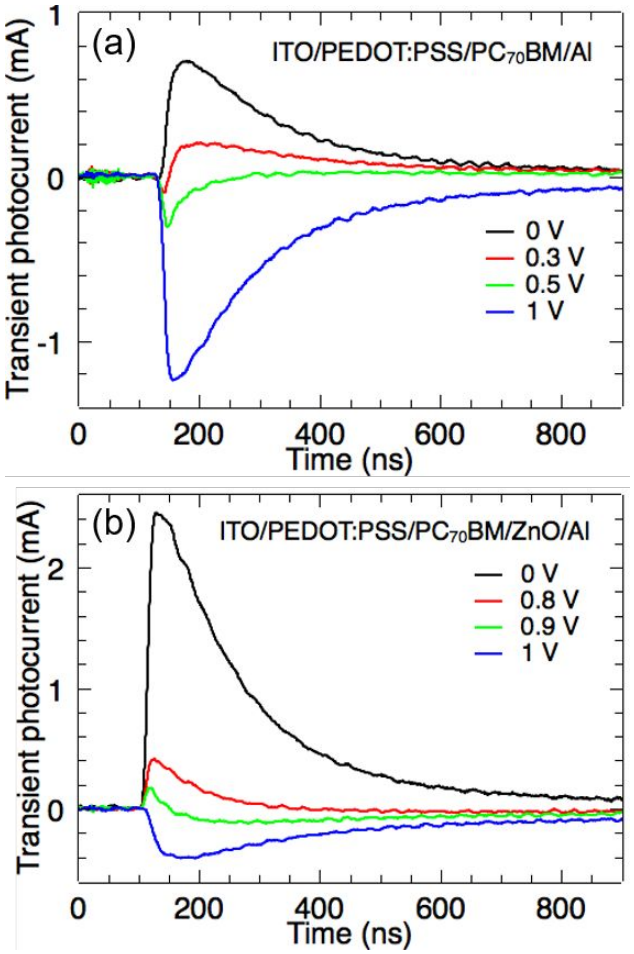


Fig. 4: Transient photocurrents measured for devices comprising layer configurations of (a) ITO/PEDOT:PSS/$PC_{70}BM$/Al and (b) ITO/PEDOT:PSS/$PC_{70}BM$/ZnO/Al under different external biases.

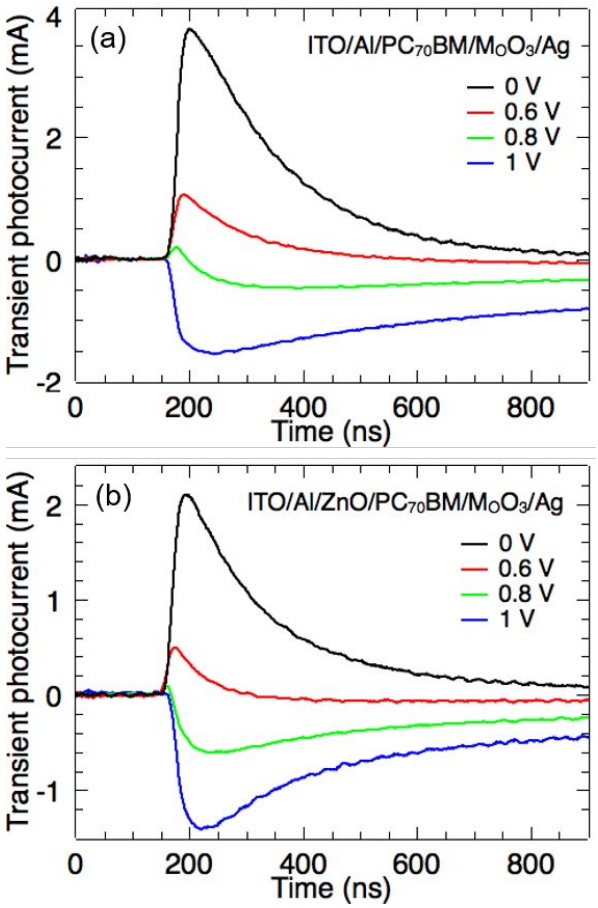


Fig. 5: Transient photocurrents measured for devices comprising layer configurations of (a) ITO/Al/$PC_{70}BM$/$M_OO_3$/Ag and (b) ITO/Al/ZnO/$PC_{70}BM$/$M_OO_3$/Ag under different external biases.

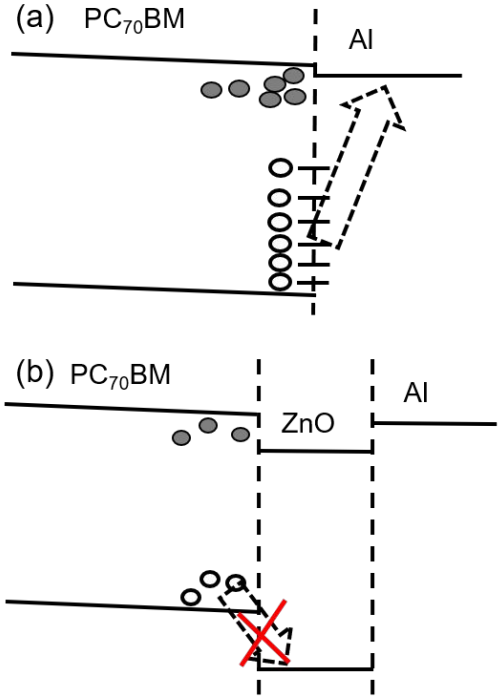


Fig. 6: Schematic diagrams illustrating the processes of interfacial exciton dissociation at the (a) organic/Al and (b) organic/ZnO/Al interfaces.

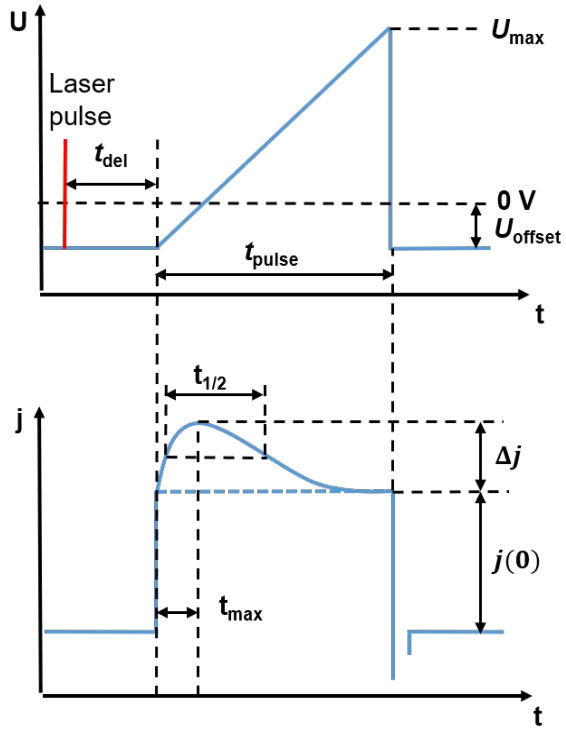


Fig. 7: Schematic illustration of the photo-CELIV method.

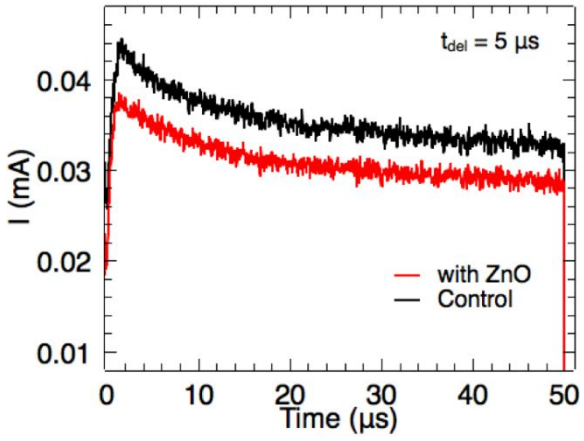


Fig. 8: Typical photo-CELIV transients measured for the OSC with a ZnO EEL and a control cell with a delay of 5 µs.

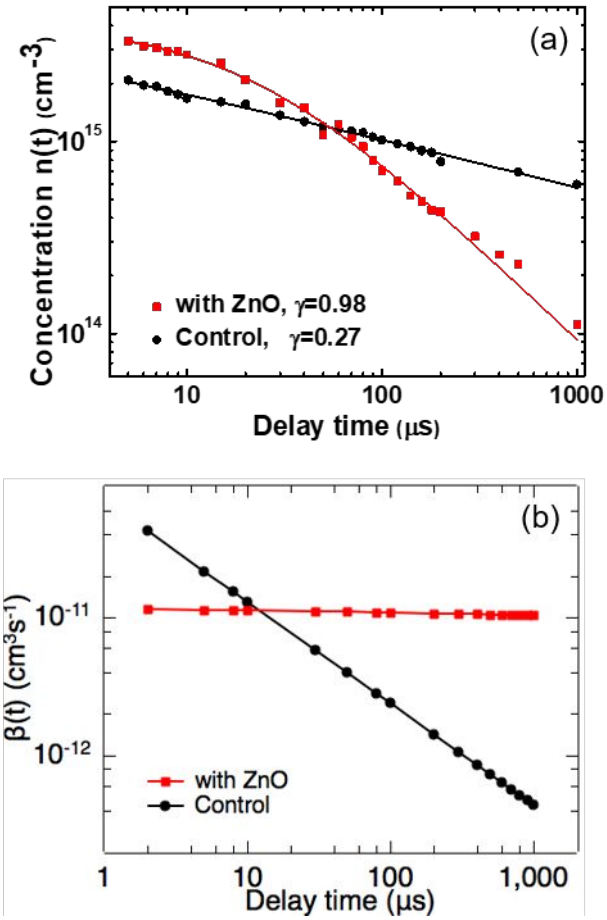


Fig. 9: Double logarithmic plots of delay time-dependent (a) carrier concentration and (b) bimolecular recombination coefficient obtained for the OSC with a ZnO EEL and a control cell.

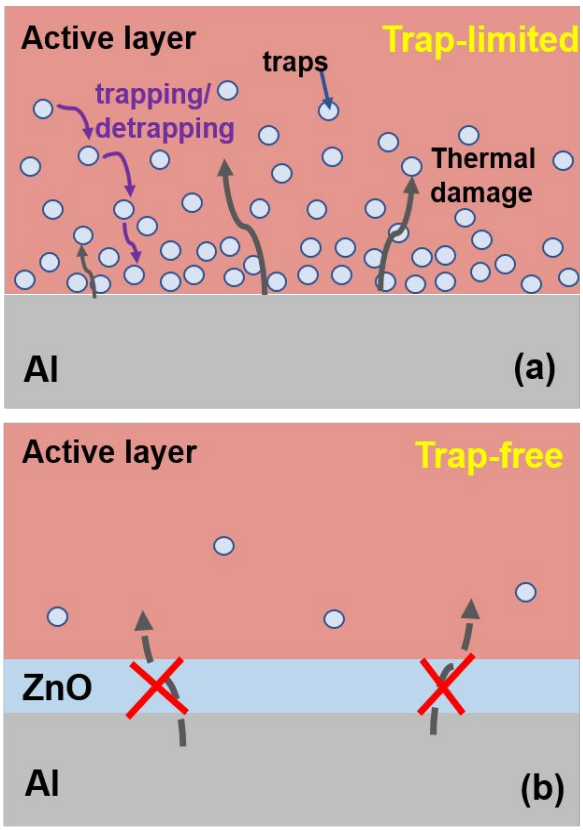


Fig. 10: Schematic diagram illustrating the multi-trap model and the distribution of the interfacial defects and traps formed at the organic/Al interface that is formed by depositing Al on (a) organic layer, and (b) on ZnO EEL-protected organic layer.

Table 1: Summary of the parameters obtained for OSCs made with and without a ZnO EEL.

| | PCE (%) | $J_{SC}$ (mA/cm$^2$) | FF (%) | $V_{OC}$ (V) | $R_S$ (Ω·cm$^2$) | $R_{SH}$ (Ω·cm$^2$) |
|---|---|---|---|---|---|---|
| with ZnO | 7.69±0.2 | 14.22±0.1 | 72.94±0.2 | 0.74 | 4.8 | 1513.8 |
| Control | 7.03±0.2 | 14.13±0.2 | 67.23±0.1 | 0.74 | 5.9 | 987.1 |

Table 2: Summary of parameters calculated using equation (3).

| | $n(0)$ (cm$^{-3}$) | $\gamma$ | $\tau_B$(μs) |
|---|---|---|---|
| ZnO/Al | $4.12\times10^{15}$ | 0.98 | 21.41 |
| Al | $1.27\times10^{15}$ | 0.26 | 0.01 |